Supporting Information

Solution-processed Two-dimensional Metal Oxide Anticorrosion Nanocoating

Leanddas Nurdiwijayanto,[†] Hiroki Nishijima,[‡] Yoshiharu Miyake,[‡] Nobuyuki Sakai,[†] Minoru Osada,[†§] Takayoshi Sasaki,[†] Takaaki Taniguchi*[†]

[†] International Center for Materials Nanoarchitectonics (WPI-MANA), National Institute for Materials Science (NIMS), Namiki 1-1, Tsukuba, Ibaraki 305-0044, Japan.

[‡] New Field Material Creation Department, Electrification & Environment Material Engineering Division, Toyota Motor Corporation, Toyota-cho, Toyota, Aichi 471-8572, Japan.

[§] Institute of Materials and Systems for Sustainability, Nagoya University, Furocho, Chikusa-ku, Nagoya 464-8603, Japan.

*Corresponding Author: TANIGUCHI.Takaaki@nims.go.jp

Additional experimental details, materials, methods, tables, and references.

Materials and Methods

Materials

Reagents such as K_2CO_3, TiO_2, Li_2CO_3, $CaCO_3$, and Nb_2O_5 (Rare Metallic Co., Ltd) have a purity of 99.9% or higher. All other analytical-grade reagents were used as received. Ultrapure water (>18 MΩ·cm) was obtained from a Milli-Q water filtration system and used during the experiment. SUS409 was chosen as a representative stainless-steel (SUS) substrate because of its widespread use in various industries. The SUS substrate was subjected to degreasing and pickling procedures prior to each experiment to remove any impurity and oxide layer on the surface.

Preparation of $Ti_{0.87}O_2$ and $Ca_2Nb_3O_{10}$ nanosheets

$Ti_{0.87}O_2$ and $Ca_2Nb_3O_{10}$ nanosheets were prepared by delaminating the corresponding potassium compounds ($K_{0.8}Ti_{1.73}Li_{0.27}O_4$ and $KCa_2Nb_3O_{10}$), according to previously reported procedures.[S1–S3] $K_{0.8}Ti_{1.73}Li_{0.27}O_4$ and $KCa_2Nb_3O_{10}$ were synthesized by solid-state calcination of a mixture of $K_2CO_3/TiO_2/Li_2CO_3$ and $K_2CO_3/CaCO_3/Nb_2O_5$ (molar ratios = 0.4:1.73:0.135 and 0.5:2:1.5) at 1000 and 1200 °C, respectively. The obtained powders were subsequently converted into their protonic forms of $H_{1.07}Ti_{1.73}O_4·H_2O$ and $HCa_2Nb_3O_{10}·1.5H_2O$ by repeated acid-exchange reactions.

The protonated oxides were then treated with aqueous tetrabutylammonium (TBA) hydroxide solutions at equivalent dosing concentrations, with respect to the exchangeable protons in the oxides ($TBA^+/H^+ = 1$) under vigorous reciprocal shaking for seven days. The prepared suspensions contained unilamellar nanosheets with an average lateral size of 1–3 μm (**Figure S1**).

Fabrication of nanosheet coating on stainless-steel (SUS 409) substrates

The colloidal nanosheets were deposited on a SUS substrate by an electrostatic layer-by-layer (LbL) self-assembly process.[S4,S5] The substrate was primed with a cationic polymer (polydiallyldimethylammonium chloride (PDDA, 100 $g \cdot dm^{-3}$, pH = 9) or polyethylenimine (PEI, 2.5 $g \cdot dm^{-3}$, pH = 9)) solution for 5 min to make their surface positively charged. The prepared substrate was subsequently dipped in a dispersion of the nanosheets (0.3 $g \cdot dm^{-3}$, pH = 9) for another 5 min, meticulously rinsed with Milli-Q water, and dried under a N_2 gas stream. The deposition process was repeated in n cycles to fabricate a desired thickness of multilayer nanosheet films. Annealing processes at 400 °C for 8 h (heating and cooling rates = 1 $°C \cdot min^{-1}$) were carried out in air and in a reduced atmosphere under a 5%H_2/Ar stream (flow rate $\approx$ 3.6 $dm^3 \cdot min^{-1}$). UV treatment on the nanosheet coating on SUS was carried out using AS-One SUV-16 Handy UV lamp (λ = 254 nm, intensity = 1~1.2 $mW \cdot cm^2$) to eliminate PDDA or PEI molecules from the nanosheet gallery. Vibration test was performed using water shaker and ultrasonication (ASU-10M cleaner). Tape peeling test was done using Nichiban Cellophane tape.

Structural characterizations

The topography of the employed nanosheets was evaluated using a Hitachi SPA 400 atomic force microscope (AFM) in the tapping mode. The nanosheets were deposited on a Si substrate using the Langmuir–Blodgett (LB) deposition technique following the previously reported procedure.[S6] All AFM images were recorded using Si cantilevers (Hitachi SI-DF20), with a spring constant of 15 $N \cdot m^{-1}$, resonance frequency of 110–150 Hz, tip height of 225 μm, and nominal tip radius of 10 nm. Nanostructures of the coated nanosheets on SUS substrates were evaluated using a transmission electron microscope (TEM), JEOL TEM-ARM300F, at an applied voltage of 200 kV. The TEM was equipped with energy-dispersive spectroscopy (EDX)

to determine the elemental distribution of the nanosheets-SUS coating. Surface morphology images of samples were recorded with a field-emission scanning electron microscope (FE-SEM), JEOL JSM-7100F, at a 1-kV applied voltage. Osmium sputter coating (Filgen OPC80T) of ~1 nm thickness was applied to the SEM specimens to avoid charging effect under the incident electron beams. X-ray photoelectron spectroscopy (XPS) analysis was performed using a PHI-5000 VersaProbe II (ULVAC-PHI) instrument with a monochromatic Al Kα source (1486.6 eV) at a take-off angle of 45° with respect to the surface, corresponding to a measurement area of ca. 1.4×0.1 mm^2. The spectra were calibrated to the C 1s binding energy (284.8 eV). Depth profiling in XPS was carried out using Ar$^+$ ions at 3 kV. The Auger electron spectra (AES) and elemental surface distribution images were recorded with a JEOL JAMP-9510F AES at 10 kV 10 mA. Depth profiling in AES was carried out using Ar$^+$ ions at 2 kV. X-ray diffraction (XRD) was carried out using a Rigaku SmartLab diffractometer with monochromatic Cu Kα radiation ($\lambda = 0.15406$ nm). The data were recorded for 2θ angles of 5°–90° at a step size of 0.01° and a scan speed of 1 deg·min^{-1}.

Salt spray corrosion test

Salt spray corrosion tests were employed to evaluate the corrosion-protection ability of SUS using a combined cyclic corrosion testing method (Suga Testing Machine Co., Ltd.: CYP-200) to achieve simulated environment control similar to outdoor exposure. The specimens were placed in a test chamber and subjected to a continuous indirect spray of a neutral saltwater solution (Japan Industrial Standard, JIS K 8150) for a certain amount of time. The wetted specimens were set to dry (60 °C, 20%–30% Rh, 4 h) to accelerate the corrosion process as the evaporated water from the exposed surface leads to an increased level of the solution concentration. The chamber was humidified (50 °C, 95% Rh, 2 h) to reliquefy the solidified corrosive substances, expecting that the corrosive liquid penetrate into the coating, thus, further

accelerating the corrosion process. The combined corrosion tests were repeated up to 20 cycles. The corrosion behaviors were evaluated from the rust formation on the steel surface and measuring the erosion pitting depth and area after rust removal.

Erosion depth and area estimation

To evaluate the depth and area of the pitting erosion, the brown rust covering the SUS surface was removed by immersion in a 10% $C_6H_8O_7 \cdot 2NH_3$ aqueous solution at 70 °C for 30–60 min, washed with water, and cleaned with a resin-made brush. The erosion depth of the corroded area was measured by the depth of a focus measurement method using an optical microscope. The displacement of focal points between the corroded and noncorroded surfaces was used to determine the erosion depth. The percentage of erosion area was determined by the ratio between the corroded parts over the total substrate area.

Potentiodynamic polarization measurement

Potentiodynamic polarization measurements were carried out according to the ASTM G5-94 standard in an aqueous 3.5 wt% NaCl solution with a Gamry electrochemical station (Gamry Interface 1010E). A standard three-electrode system was adopted, where the coated SUS coupon, a coiled Pt wire, and an Ag/AgCl (3M NaCl) electrode served as the working electrode, the counter electrode, and the reference electrode, respectively. The SUS coupon was set in a Teflon-made evaluating cells equipped with an O-ring holder (Plate material evaluating cell, ALS Co., Ltd.). A 6 mm hole spacer made of a Kapton tape (thickness = 0.1~0.2 mm) was placed in between the coupon and the O-ring holder to avoid coating damage during tightening. The potentiodynamic polarization measurements were performed on the sample polarized at ±250 mV with respect to its OCP at a scan rate of 0.167 mV·s^{-1} after the systems reached their steady-state condition (stable OCP) for at least 60 min. The resulting potentiodynamic

polarization curves provide important corrosion information such as corrosion potential (E_{corr}) and corrosion current (I_{corr}), where they were extracted from the intersection point of the linear fit of the polarization data.[S7] The corrosion rate (CR) was then estimated using the following equation:[S8,S9]

$$CR = \frac{I_{corr} \times K \times EW}{\rho A},\tag{1}$$

where K is the CR constant (=3272 mm·year^{-1}), EW is the equivalent weight (=27.56 g for Fe), ρ is the material density (=7.76 g·cm^3), and A is the measured specimen area (=0.28 cm^2). The inhibition efficiency (IE) was calculated to evaluate the corrosion-protection efficiency of the coating layers of nanosheets using the following equation:

$$IE(\%) = \left(1 - \frac{I_{corr_{coated}}}{I_{corr_{uncoated}}}\right) \times 100\% = \left(1 - \frac{CR_{coated}}{CR_{uncoated}}\right) \times 100\%\tag{2}$$
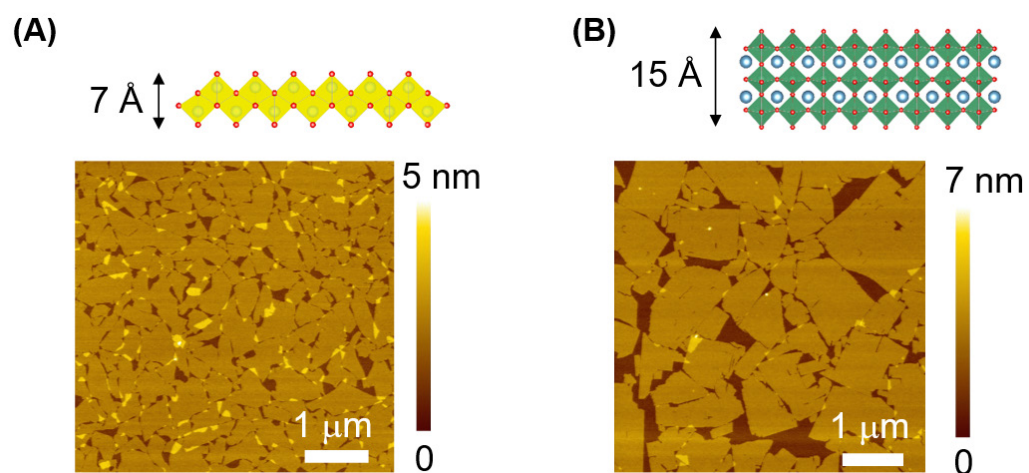
Figure S1. Schematic illustrations of 2D crystal structures and atomic force microscope (AFM) images of exfoliated unilamellar (**A**) titania ($Ti_{0.87}O_2$) and (**B**) calcium niobate ($Ca_2Nb_3O_{10}$) nanosheets.

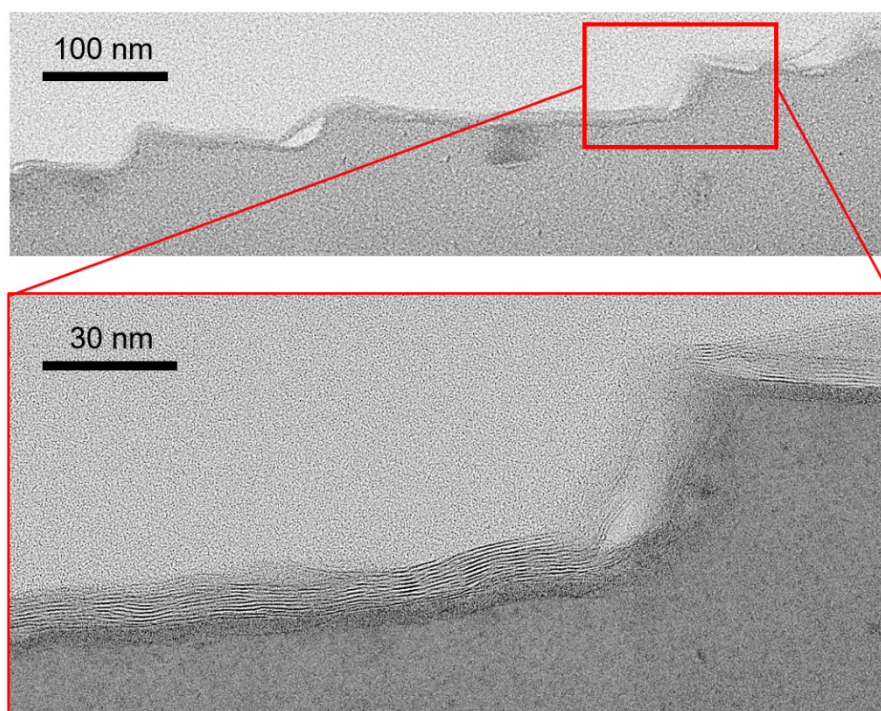**Figure S2.** TEM images of five-cycle $Ti_{0.87}O_2$ coating, displaying a high degree of flexibility of nanosheets, enabling them to adhere well even to the surface with an angle of nearly 90°.
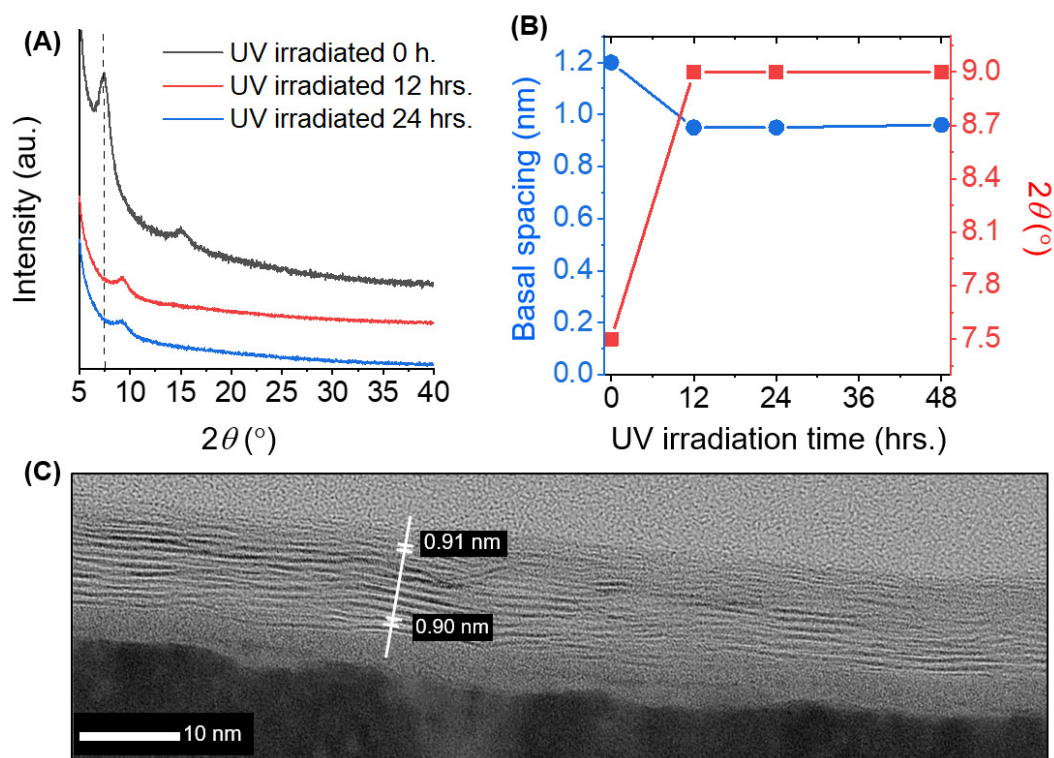
Figure S3. (**A**) XRD patterns of five-cycle $Ti_{0.87}O_2$ coatings for different UV irradiation times, showing diffraction peaks from basal spacing of $Ti_{0.87}O_2$ layers at $2\theta = 5\text{-}10°$. (**B**) Summary of basal spacing (*d*-space) values of $Ti_{0.87}O_2$ coating layers calculated from 2θ of the XRD data in (**A**). (**C**) Cross-sectional HR-TEM image of the $Ti_{0.87}O_2$ coating layer after 12 h of UV light irradiation.
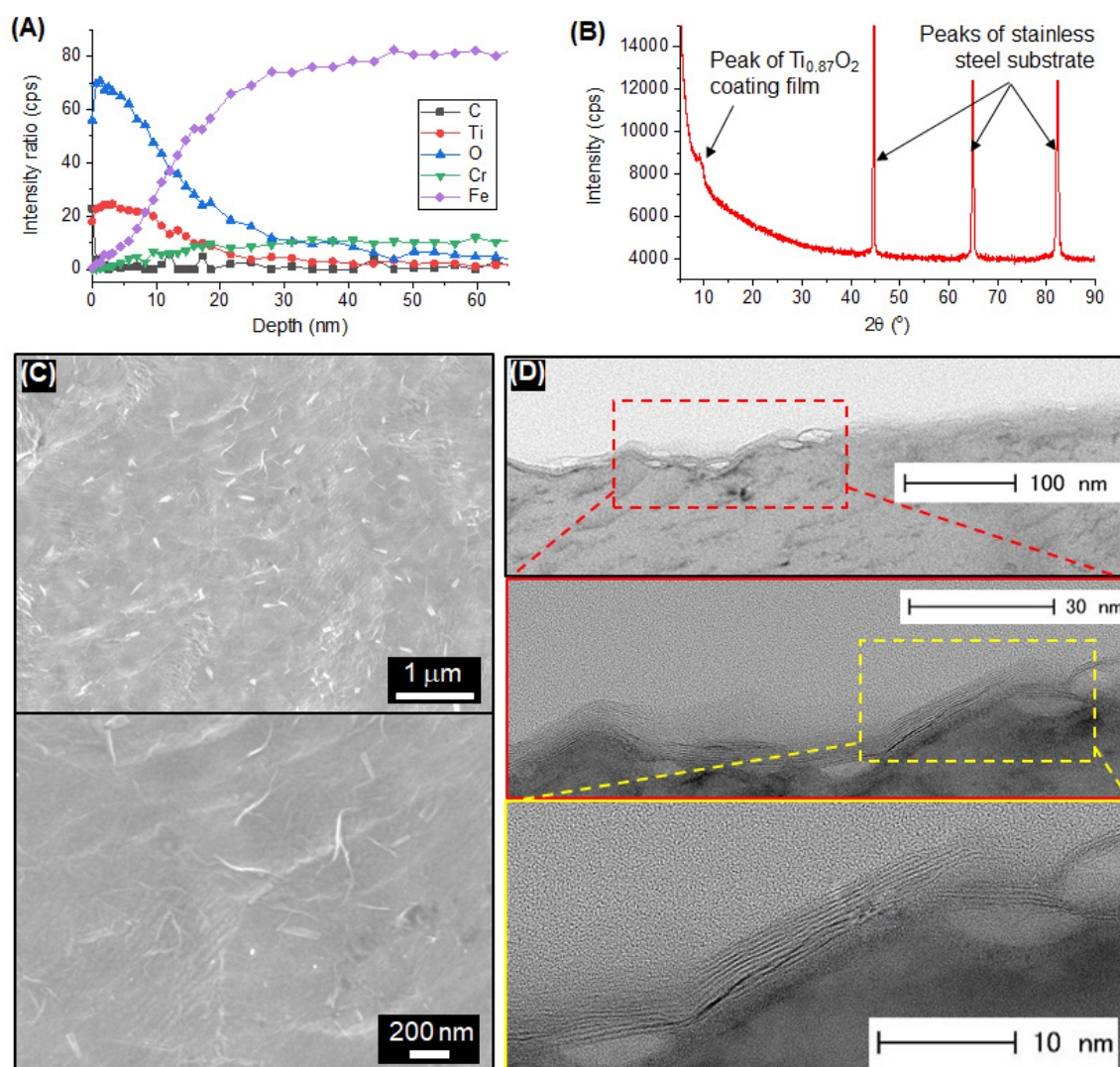
Figure S4. (**A**) Depth profile analysis by XPS and (**B**) XRD data of 5L-$Ti_{0.87}O_2$/SUS after vibration tests by water shaking and ultrasonication in water, suggesting the lamellar structure of $Ti_{0.87}O_2$ coating after the tests as indicated by a peak at a diffraction angle around 10°, corresponding to the stacking distance of $Ti_{0.87}O_2$ layers. (**C**) Corresponding surface morphology (top: low-, bottom: high-magnification) and (**D**) cross-sectional TEM images, confirming that $Ti_{0.87}O_2$ nanosheets remain intact with the metal substrate.
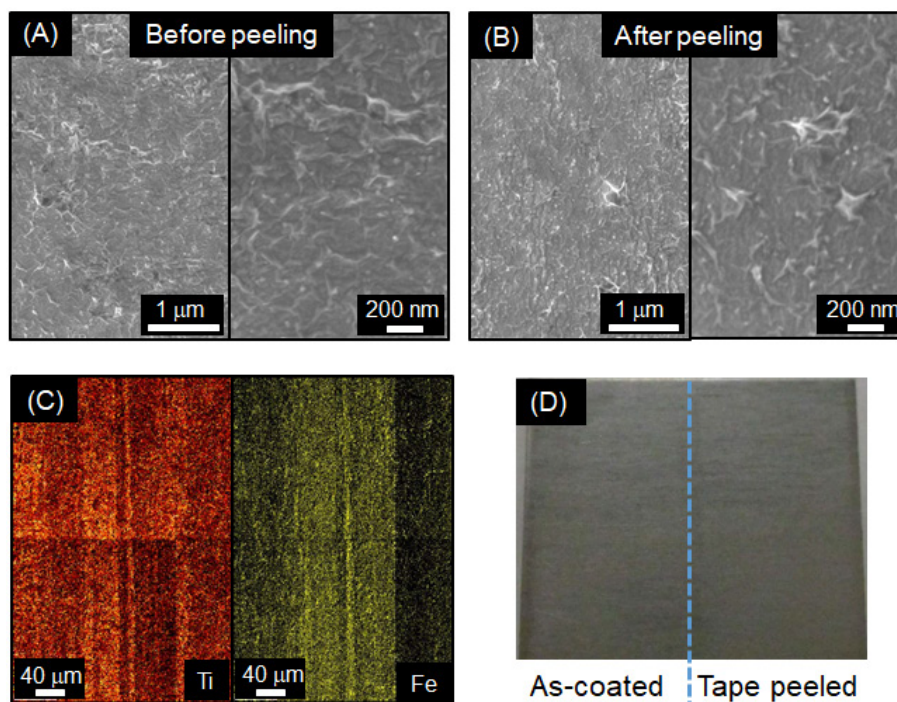
Figure S5. Tape peeling test of fabricated $Ti_{0.87}O_2$-SUS, suggesting that the coated $Ti_{0.87}O_2$ layers remain intact with the metal substrate as indicated SEM observation by (**A**) before and (**B**) after tape peeling test. (**C**) AES elemental mapping of tape peeled region. (**D**) Photograph of $Ti_{0.87}O_2$-SUS displaying as-coated and tape-peeled regions of $Ti_{0.87}O_2$-SUS.
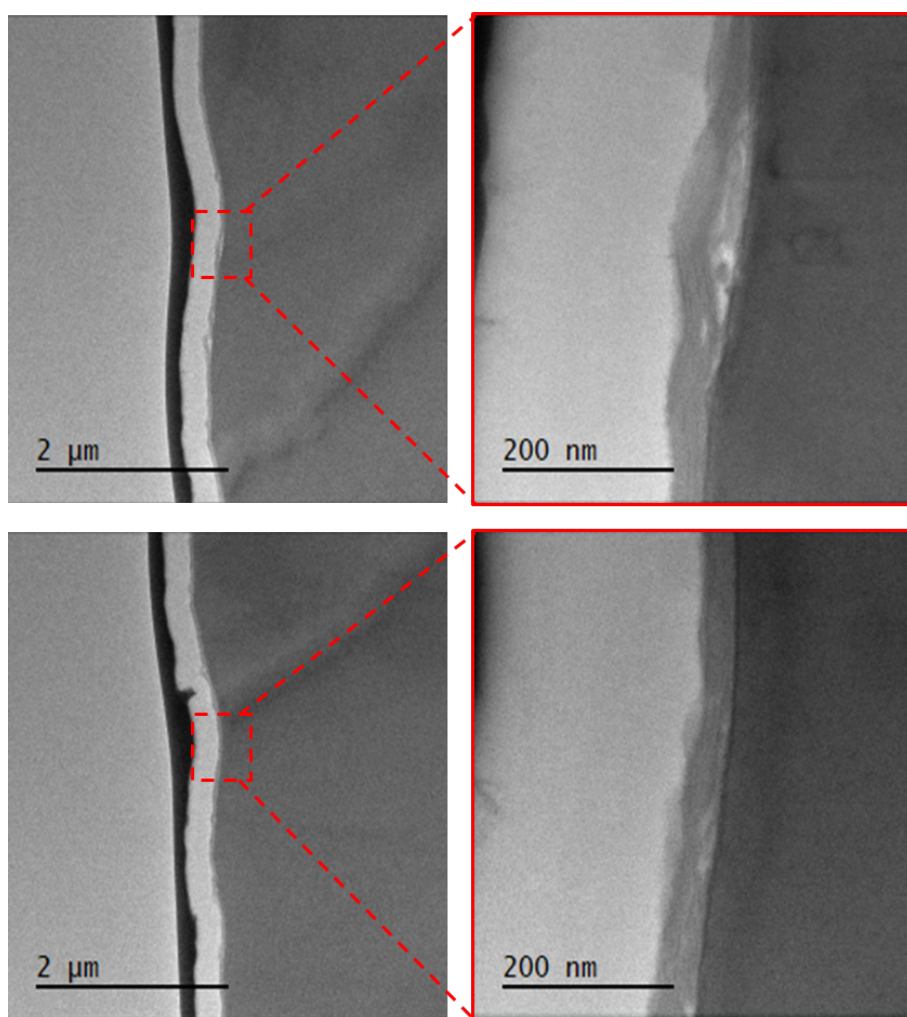
Figure S6. TEM images of the $Ti_{0.87}O_2$ film fabricated from 20 LbL cycles, displaying uniform film formation at ca. 50-nm-thick assembled nanosheet layers.
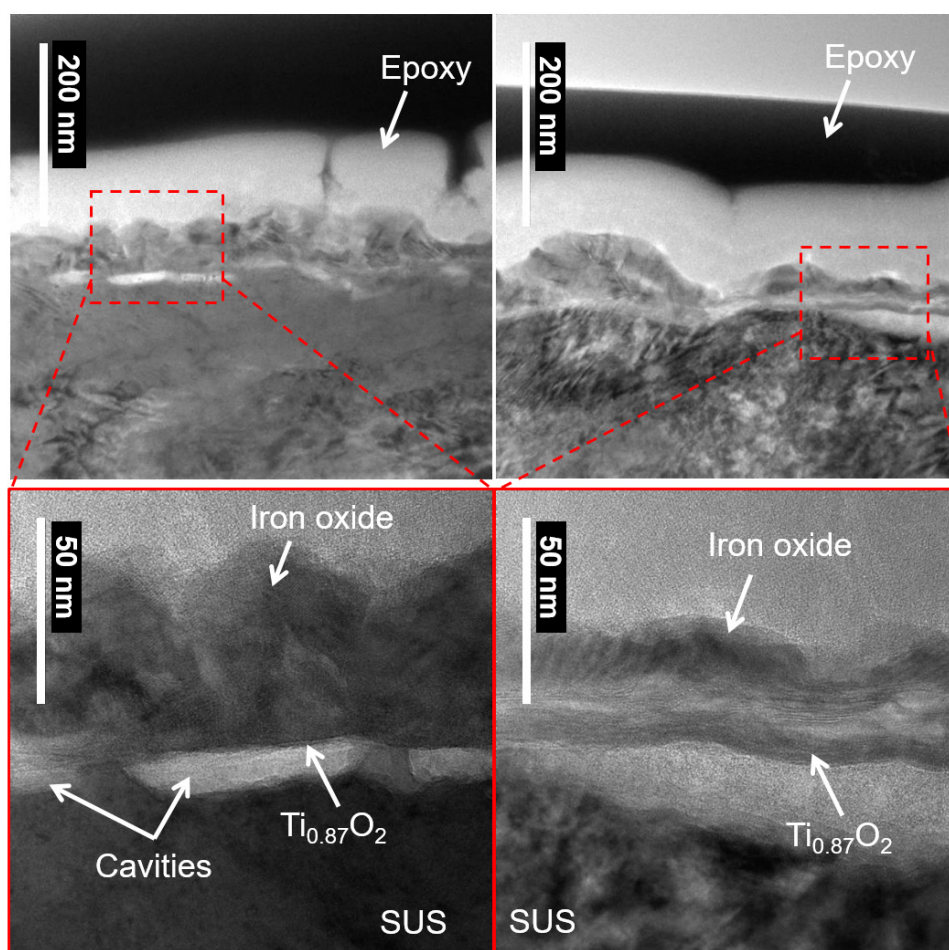
Figure S7. TEM images of $Ti_{0.87}O_2$-SUS annealed at 400 °C under air conditions for two different selected areas.
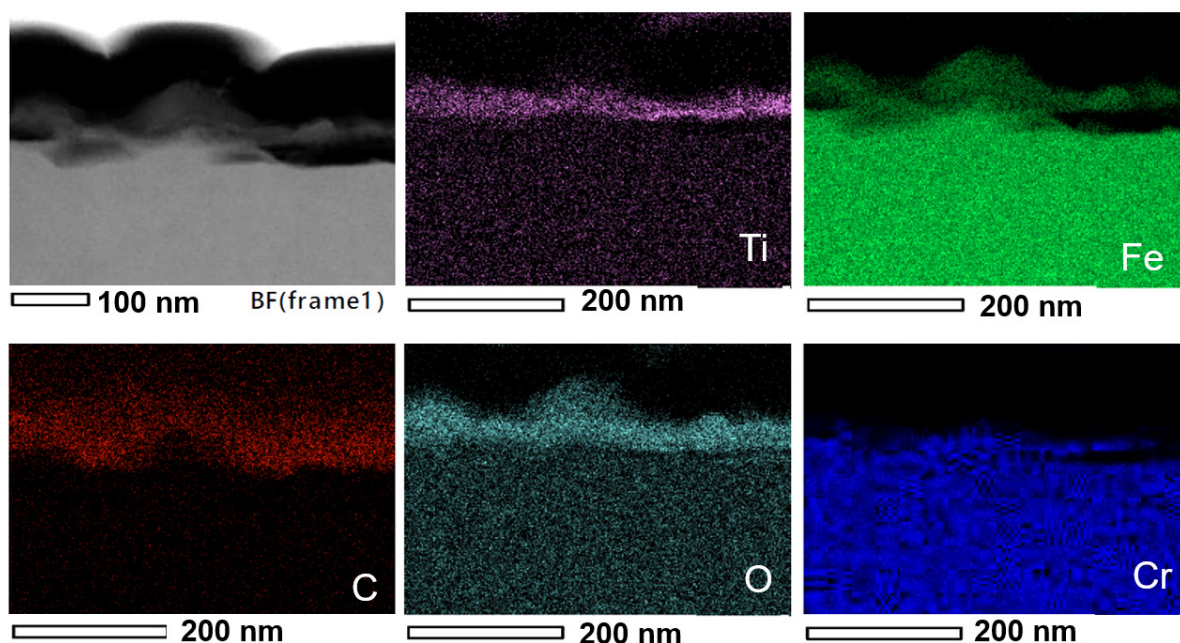
Figure S8. Elemental mapping distribution of $Ti_{0.87}O_2$-SUS annealed at 400 °C in the air. The emergence of grains on the annealed $Ti_{0.87}O_2$ layers and cavities for the $Ti_{0.87}O_2$/SUS interface were identified (**Figure S7**). Elemental distribution mapping analysis indicates that the grains consisting of iron oxides (**Figure S8**) thermally penetrate the $Ti_{0.87}O_2$ layers during the heat treatment by oxidation.
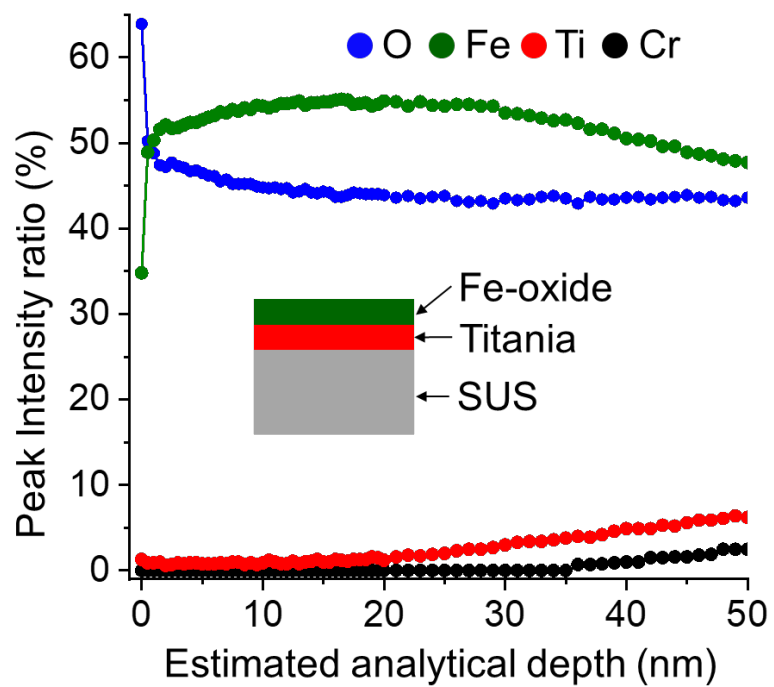
Figure S9. XPS depth profiling elemental data of $Ti_{0.87}O_2$-SUS annealed at 400 °C in air.
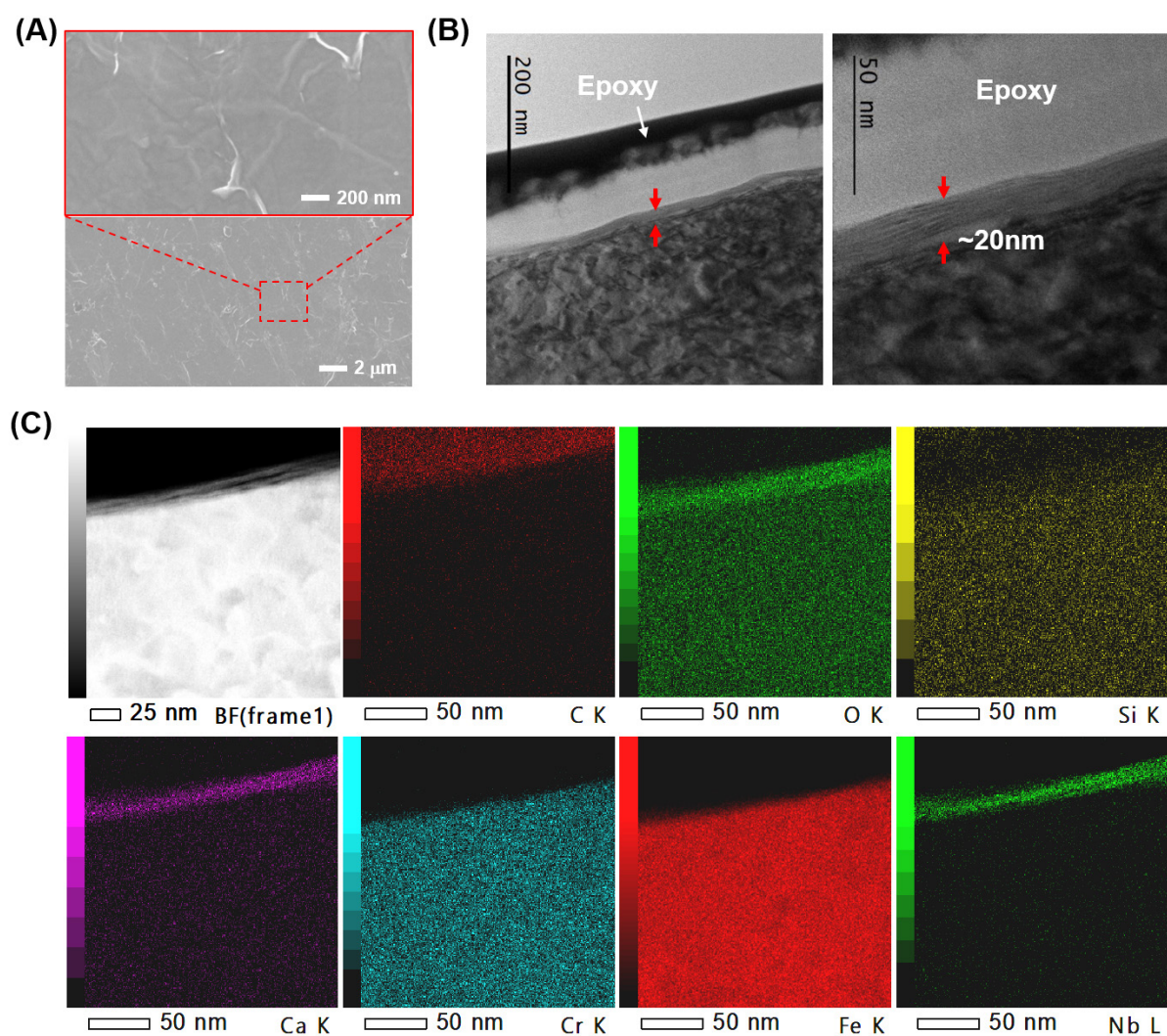
Figure S10. Development of five-cycle CNO coating on SUS. (**A**) SEM image indicating uniform film formation without noticeable defects. (**B**) Corresponding TEM images showing a uniform thickness of ca. 20 nm. (**C**) Elemental mapping distribution confirms the deposition of CNO layers on the SUS substrate.
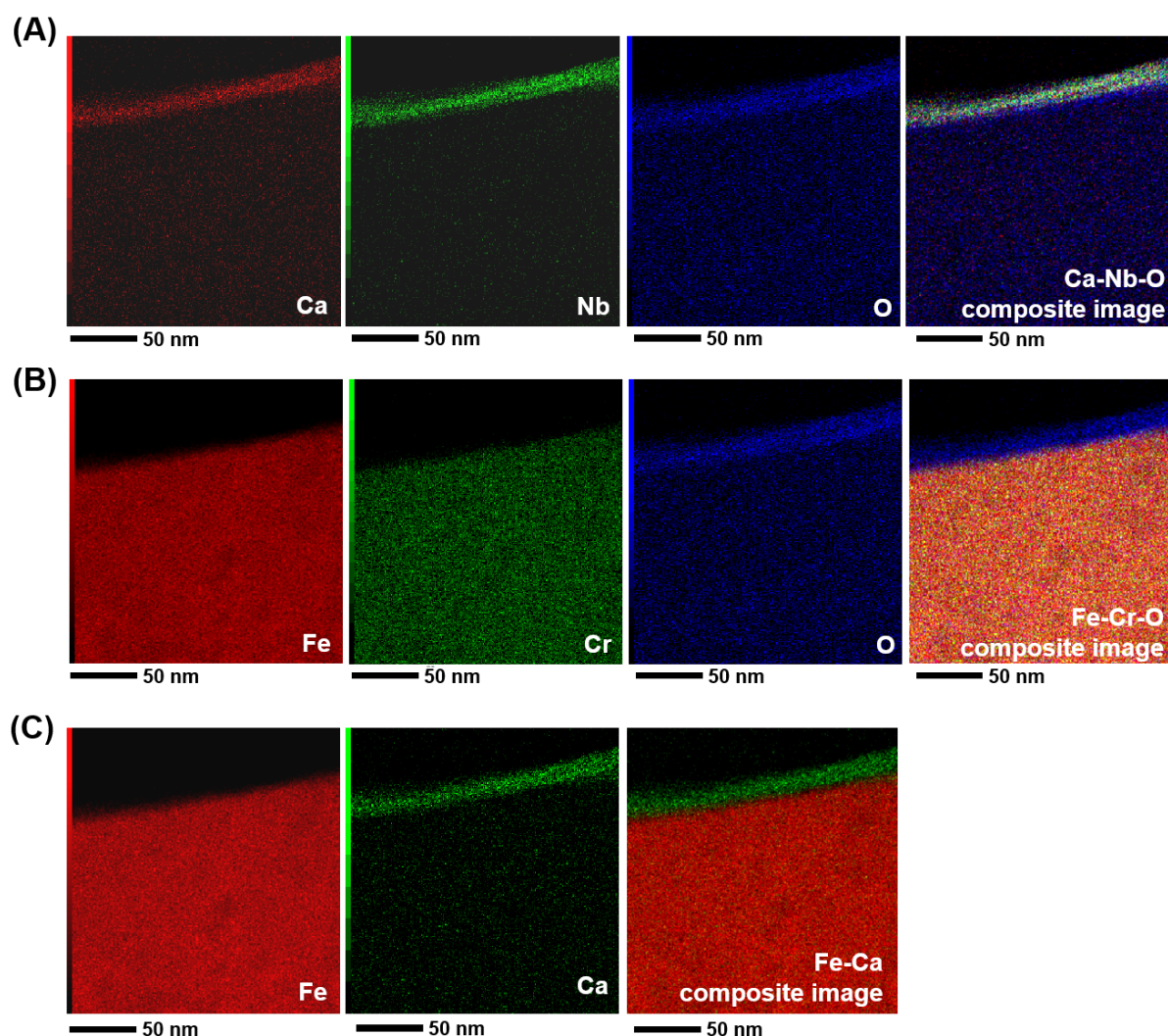
Figure S11. In-depth analysis of elemental mapping distribution from composite images of as-fabricated CNO-SUS anticorrosion protective coating. (**A**) Ca–Nb–O, (**B**) Fe–Cr–O, and (**C**) Fe–Ca. Analysis of the composite images helps in evaluating film quality after the deposition process. The CNO layers firmly adhere to the SUS substrate. The damage and defect on the SUS substrate could not be identified.
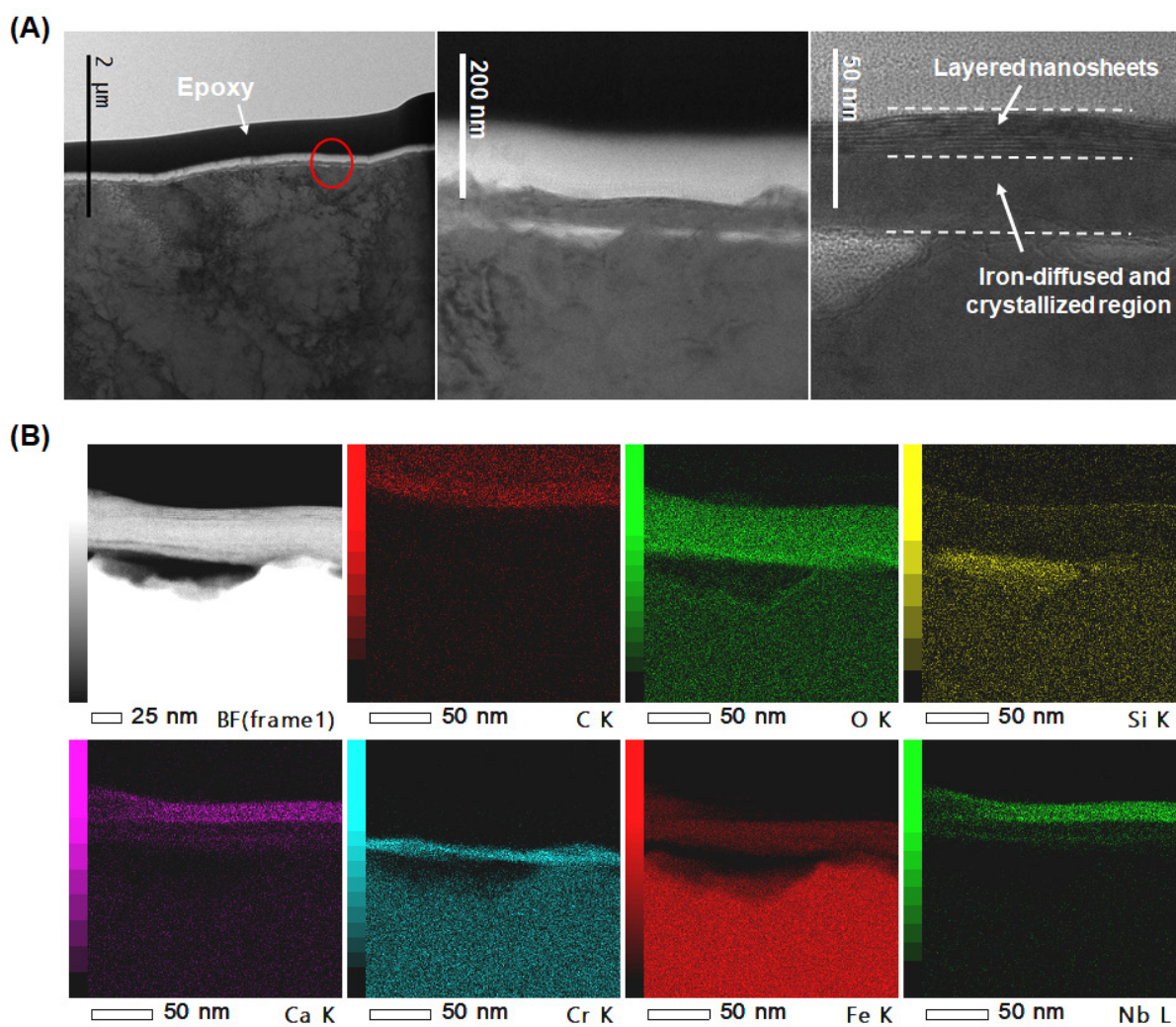
Figure S12. (**A**) TEM images of annealed CNO-SUS at 400 °C in the air. (**B**) Elemental mapping distribution of CNO-SUS at 400 °C.

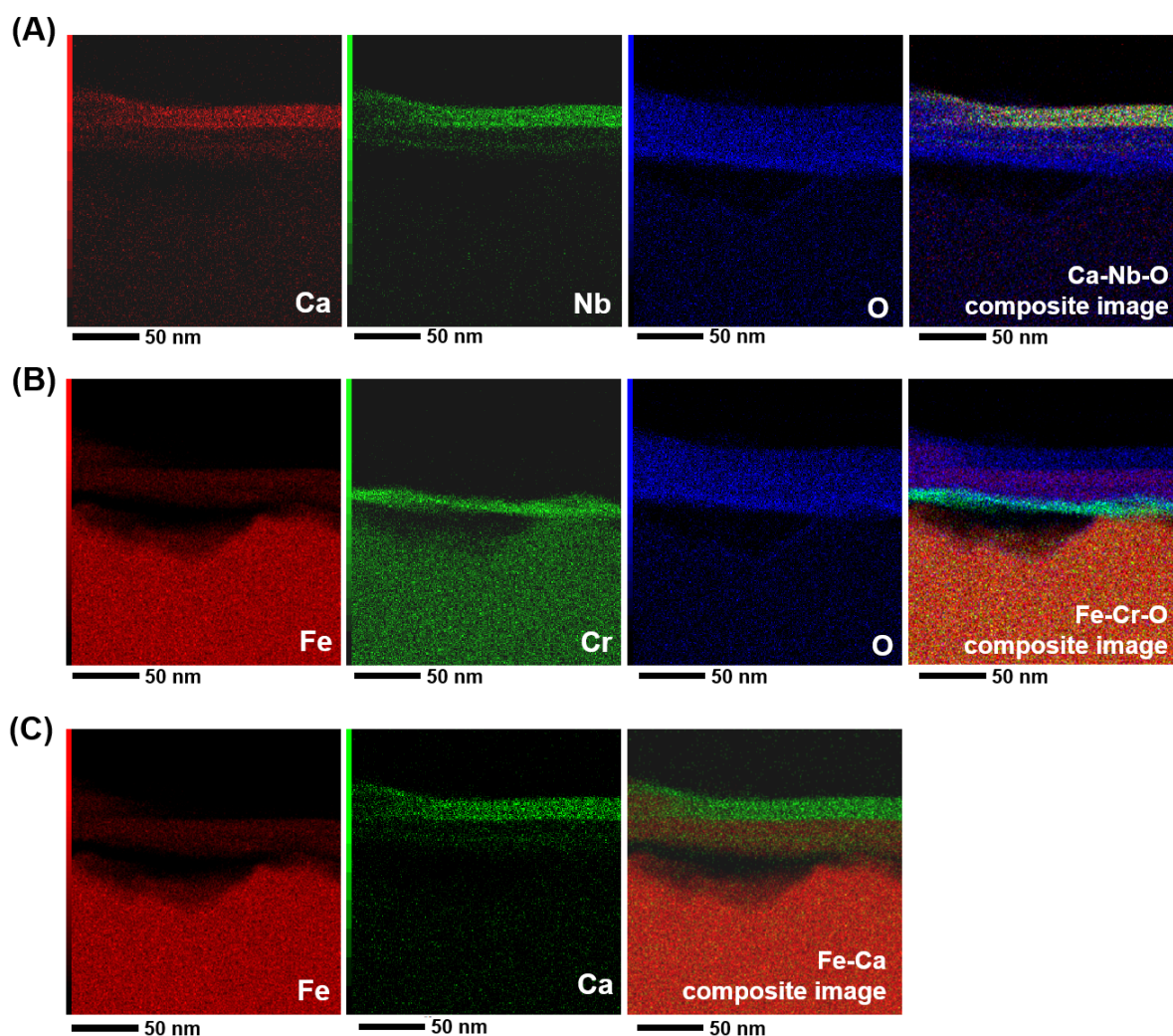**Figure S13.** In-depth analysis of elemental mapping distribution of annealed CNO-SUS at 400 °C in the air. (**A**) Ca–Nb–O, (**B**) Fe–Cr–O, and (**C**) Fe–Ca. Chromium oxide layer is found under the iron oxide layer.

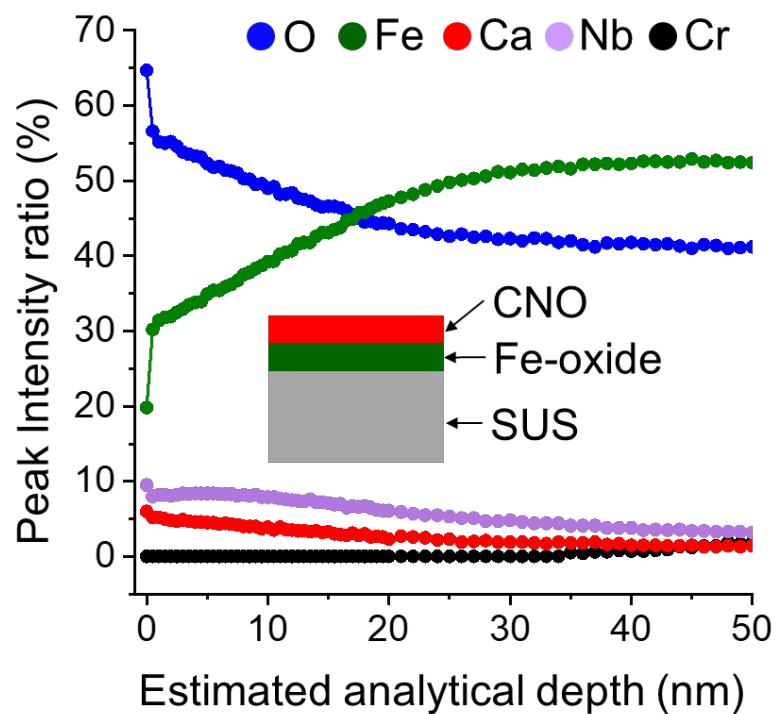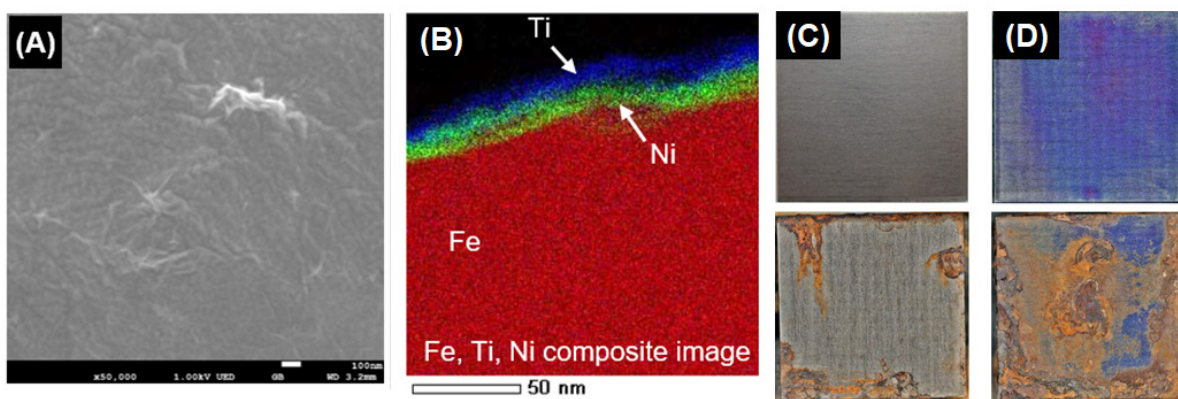**Figure S14.** XPS depth profiling elemental data of CNO-SUS annealed at 400 °C in air.

Figure S15. (**A**) Surface morphology of five-cycle $Ti_{0.87}O_2$ coating on Ni-plated SUS. (**B**) Corresponding cross-sectional TEM-EDX elemental mapping images. Photograph of $Ti_{0.87}O_2$-modified Ni-plated SUS (**C**) with and (**D**) without heat treatment at 400 °C in the air (top: before, bottom: after salt spray tests).

Table S1. Comparison of inhibition efficiency (IE) among different coatings and metal substrates deducted from potentiodynamic tests.

Substrate	Coating	Thickness (μm)	I_{corr} (A·cm^{-2})	I_{corr}(coated)/I_{corr}(uncoated)	IE (%)	Ref.
Graphene-based coating						
Carbon steel	Epoxy/Polyurethane/GO	300	7.8×10^{-10}	0.0002	99.98	S10
Mild steel	Epoxy/GO	150	2.2×10^{-7}	0.0151	98.49	S11
Galvanized iron	GO	150	7.5×10^{-6}	0.2339	76.61	S12
Cold-rolled steel	Epoxy/GO	110	1.0×10^{-7}	0.0067	99.33	S13
Carbon steel	Acrylic/Graphene	30	2.9×10^{-8}	0.0530	94.70	S14
Carbon steel	Epoxy/GO	17	6.0×10^{-8}	0.0070	99.30	S15
Stainless steel	Electrodeposited GO	2	9.5×10^{-8}	0.0646	93.54	S16
Copper	1L Graphene	~0.0005	N/A	N/A	86.37	S7
Copper	2L Graphene	~0.001	4.8×10^{-6}	0.2227	77.73	S17
hBN-based coating						
Stainless steel	Epoxy/hBN	30	8.1×10^{-7}	0.0105	98.95	S18
Carbon steel	Epoxy/hBN/Graphene	20	5.6×10^{-9}	0.0001	99.99	S19
Copper	1L hBN	~0.0005	1.2×10^{-8}	0.0400	96.00	S20

Oxide-based atomic layer deposition (ALD)

Stainless steel	HfO$_2$ ALD	0.036	3.6×10^{-10}	0.0033	99.67	S21
Stainless steel	HfO$_2$ Plasma-enhanced ALD	0.036	5.2×10^{-11}	0.0005	99.95	S21
Stainless steel	Al$_2$O$_3$ ALD	0.050	2.4×10^{-10}	0.0003	99.97	S22
Stainless steel	Ta$_2$O$_5$ ALD	0.050	1.2×10^{-9}	0.0014	99.86	S22
Stainless steel	TiO$_2$ ALD	0.058	6.3×10^{-8}	0.0900	91.00	S23
Stainless steel	CrN/TiO$_2$ ALD	0.170	3.1×10^{-7}	0.1192	88.08	S24
Stainless steel	Al$_2$O$_3$/TiO$_2$ ALD	0.420	1.0×10^{-9}	0.0100	99.00	S25

Other oxides and alloys: sol-gel, electrodeposition, polymer composites

Cold-rolled steel	H$_2$ZrF$_6$	0.060	5.1×10^{-6}	0.3517	64.83	S26
Carbon steel	Polyethylenimine/Tanic acid	0.210	1.1×10^{-6}	0.2727	72.73	S27
Carbon steel	TiO$_2$/SiO$_2$ composites	1	4.9×10^{-7}	0.1021	89.79	S28
Carbon steel	Y-Al$_2$O$_3$	2.2	1.5×10^{-5}	0.0977	90.23	S29
Mild steel	ZnNi alloy	13	1.6×10^{-6}	0.2133	78.67	S30
Carbon steel	ZnO/Polyurethane	20	4.9×10^{-5}	0.0030	99.70	S31
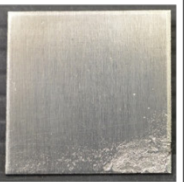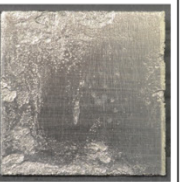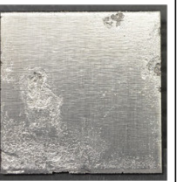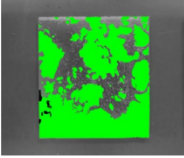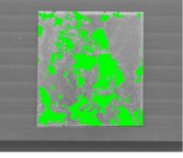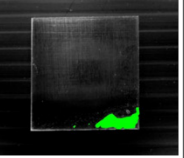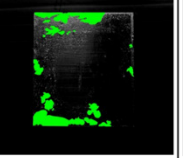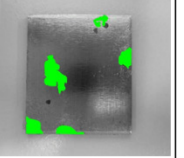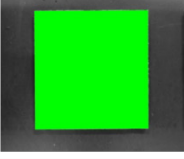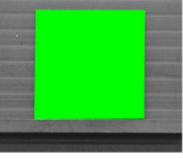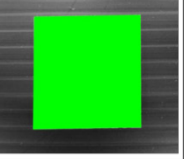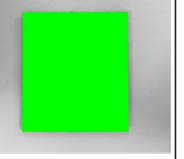
Carbon steel	Co–Al$_2$O$_3$	26	8.0×10^{-7}	0.0533	94.67	S32
Stainless steel	Ni–Cr–Al$_2$O$_3$	250	8.0×10^{-8}	0.0075	99.25	S33

Table S2. Tafel parameters (corrosion potential (E_{corr}) and current potential (I_{corr})), corrosion rate (CR), and inhibition efficiency (IE) of coated SUS in 3.5 wt% NaCl solution.

Samples	E_{corr} ($V_{Ag/AgCl}$)	I_{corr} ($A \cdot cm^{-2}$)	I_{corr}(coated)/I_{corr}(uncoated)	CR ($mm \cdot year^{-1}$)	IE (%)
SUS (bare uncoated)	−0.091	5.85×10^{-6}	N/A	6.79×10^{-2}	N/A
SUS (400 °C)	−0.353	7.43×10^{-6}	N/A	8.63×10^{-2}	N/A
$Ti_{0.87}O_2$-SUS	0.026	4.58×10^{-9}	0.0008[*]	5.32×10^{-5}	99.92[*]
$Ti_{0.87}O_2$-SUS (400 °C)	−0.322	4.96×10^{-6}	0.6686[**]	5.77×10^{-2}	33.14[**]
CNO-SUS (As-depo)	0.031	6.69×10^{-9}	0.0011[*]	7.77×10^{-5}	99.89[*]
CNO-SUS (400 °C)	−0.291	6.62×10^{-7}	0.892[**]	7.69×10^{-3}	91.08[**]
H_2-CNO-SUS (H₂ preannealed)	−0.036	5.39×10^{-8}	0.0073[**]	6.26×10^{-4}	99.27[**]
H_2-CNO-SUS (400 °C)	−0.168	3.33×10^{-7}	0.0448[**]	3.87×10^{-3}	95.52[**]

[*] The I_{corr} and IE were compared to that of uncoated SUS. [**] The I_{corr} and IE were compared to that of annealed bare SUS (400 °C in air).

Table S3. Method for determining erosion area.

	SUS (400 °C)	Ti$_{0.87}$O$_2$-SUS (400 °C)	CNO-SUS (As deposited)	CNO-SUS (400 °C)	H$_2$-CNO-SUS (400 °C)
Rust-cleaned specimens					
Measured corroded area					
Measured total area					
Corroded area (px^2)	5.63	3.08	0.35	1.26	0.84
Total area (px^2)	8.99	8.98	9.01	9.13	9.34
% Corroded area	62.6%	34.3%	3.9%	13.8%	9.1%

References

(S1) Sasaki, T.; Kooli, F.; Iida, M.; Michiue, Y.; Takenouchi, S.; Yajima, Y.; Izumi, F.; Chakoumakos, B. C.; Watanabe, M. A mixed alkali metal titanate with the lepidocrocite-like layered structure. Preparation, crystal structure, protonic form, and acid−base intercalation properties. *Chem. Mater.* **1998**, 10, 4123–4128.

(S2) Ebina, Y.; Sasaki, T.; Watanabe, M. Study on exfoliation of layered perovskite-type niobates. *Solid State Ion.* **2002**, 151, 177–182.

(S3) Ebina, Y.; Akatsuka, K.; Fukuda, K.; Sasaki, T. Synthesis and in situ X-ray diffraction characterization of two-dimensional perovskite-type oxide colloids with a controlled molecular thickness. *Chem. Mater.* **2012**, 24, 4201–4208.

(S4) Decher, G. Fuzzy nanoassemblies: Toward layered polymeric multicomposites. *Science.*

1997, 277, 1232–1237.

(S5) Sasaki, T.; Ebina, Y.; Tanaka, T.; Harada, M.; Watanabe, M.; Decher, G. Layer-by-layer assembly of Titania nanosheet/polycation composite films. *Chem. Mater.* **2001**, 13, 4661–4667.

(S6) Akatsuka, K.; Haga, M. A.; Ebina, Y.; Osada, M.; Fukuda, K.; Sasaki, T. Construction of highly ordered lamellar nanostructures through langmuir-blodgett deposition of molecularly thin Titania nanosheets tens of micrometers wide and their excellent dielectric properties. *ACS Nano.* **2009**, 3, 1097–1106.

(S7) Prasai, D.; Tuberquia, J. C.; Harl, R. R.; Jennings, G. K.; Rogers, B. R.; Bolotin, K. I. Graphene: Corrosion-inhibiting coating. *ACS Nano.* **2012**, 6, 1102–1108.

(S8) Buchanan, R. A.; Stansbury, E. E. "Electrochemical corrosion" in *Handbook of Environmental Degradation of Materials*, ed. 2 (Ed.: Kutz, M.) Elsevier, Oxford, **2012**, pp. 87–125.

(S9) Hiromoto, S. "Corrosion of metallic biomaterials" in *Metals for Biomedical Devices*, ed. 2 (Ed.: Niinomi, M.) Elsevier, Duxford, **2010**, pp. 99–121.

(S10) Dutta, D.; Ganda, A. N. F.; Chih, J. K.; Huang, C. C.; Tseng, C. J.; Su, C. Y. Revisiting graphene–polymer nanocomposite for enhancing anticorrosion performance: A new insight into interface chemistry and diffusion model. *Nanoscale.* **2018**, 10, 12612–12624.

(S11) Pourhashem, S.; Vaezi, M. R.; Rashidi, A.; Bagherzadeh, M. R. Exploring corrosion protection properties of solvent based epoxy-graphene oxide nanocomposite coatings on mild steel. *Corros. Sci.* **2017**, 115, 78–92.

(S12) Krishnamoorthy, K.; Jeyasubramanian, K.; Premanathan, M.; Subbiah, G.; Shin, H. S.; Kim, S. J. Graphene oxide nanopaint. *Carbon.* **2014**, 72, 328–337.

(S13) Chang, K.-C.; Hsu, M.-H.; Lu, H.-I.; Lai, M.-C.; Liu, P.-J.; Hsu, C.-H.; Ji, W.-F.; Chuang, T.-L.; Wei, Y.; Yeh, J.-M.; Liu, W.-R. Room-temperature cured hydrophobic

epoxy/graphene composites as corrosion inhibitor for cold-rolled steel. *Carbon.* **2014**, 66, 144–153.

(S14) Zhu, K.; Li, X.; Wang, H.; Li, J.; Fei, G. Electrochemical and anti-corrosion behaviors of water dispersible graphene/acrylic modified alkyd resin latex composites coated carbon steel. *J. Appl. Polym. Sci.* **2017**, 134, 44445.

(S15) Zhang, Y.; Tian, J.; Zhong, J.; Shi, X. Thin nacre-biomimetic coating with super-anticorrosion performance. *ACS Nano.* **2018**, 12, 10189–10200.

(S16) Ho, C. Y.; Huang, S. M.; Lee, S. T.; Chang, Y. J. Evaluation of synthesized graphene oxide as corrosion protection film coating on steel substrate by electrophoretic deposition. *Appl. Surf. Sci.* **2019**, 477, 226–231.

(S17) Wu, W.; Liu, P.; Chen, X.; Fan, J.; Chen, S.; Liang, D. The synthesis of graphene coated copper from PMMA and the anticorrosion performance of copper substrate. *Mater. Res. Express.* **2020**, 7, 016591.

(S18) Pan, D.; Zhang, X.; Yang, G.; Shang, Y.; Su, F.; Hu, Q.; Patil, R. R.; Liu, H.; Liu, C.; Guo, Z. Thermally conductive anticorrosive epoxy nanocomposites with tannic acid-modified boron nitride nanosheets. *Ind. Eng. Chem. Res.* **2020**, 59, 20371–20381.

(S19) Ding, J.; Zhao, H.; Xu, B.; Zhao, X.; Su, S.; Yu, H. Superanticorrosive graphene nanosheets through π deposition of boron nitride nanodots. *ACS Sustain. Chem. Eng.* **2019**, 7, 10900–10911.

(S20) Mahvash, F.; Eissa, S.; Bordjiba, T.; Tavares, A. C.; Szkopek, T.; Siaj, M.; Corrosion resistance of monolayer hexagonal boron nitride on copper. *Sci. Rep.* **2017**, 7, 42139.

(S21) Li, M.; Jin, Z. X.; Zhang, W.; Bai, Y. H.; Cao, Y. Q.; Li, W. M.; Wu, D.; Li, A. D. Comparison of chemical stability and corrosion resistance of group IV metal oxide films formed by thermal and plasma-enhanced atomic layer deposition. *Sci. Rep.* **2019**, 9, 10438.

(S22) Díaz, B.; Światowska, J.; Maurice, V.; Seyeux, A.; Normand, B.; Härkönen, E.; Ritala, M.; Marcus, P. Electrochemical and time-of-flight secondary ion mass spectrometry analysis of ultra-thin metal oxide (Al_2O_3 and Ta_2O_5) coatings deposited by atomic layer deposition on stainless steel. *Electrochim. Acta* **2011**, 56, 10516–10523.

(S23) Shan, C. X.; Hou, X.; Choy, K.-L. Corrosion resistance of TiO_2 films grown on stainless steel by atomic layer deposition. *Surf. Coat. Technol.* **2008**, 202, 2399–2402.

(S24) Shan, C. X.; Hou, X.; Choy, K.-L.; Choquet, P. Improvement in corrosion resistance of CrN coated stainless steel by conformal TiO_2 deposition. *Surf. Coat. Technol.* **2008**, 202, 2147–2151.

(S25) Marin, E.; Lanzutti, A.; Guzman, L.; Fedrizzi, L. Corrosion protection of AISI 316 stainless steel by ALD alumina/titania nanometric coatings. *J. Coat. Technol. Res.* **2011**, 8, 655–659.

(S26) Eivaz Mohammadloo, H.; Sarabi, A. A.; Sabbagh Alvani, A. A.; Sameie, H.; Salimi, R. Nano-ceramic hexafluorozirconic acid based conversion thin film: Surface characterization and electrochemical study. *Surf. Coat. Technol.* **2012**, 206, 4132–4139.

(S27) Koerner, C. M.; Hopkinson, D. P.; Ziomek-Moroz, M. E.; Rodriguez, A.; Xiang, F. Environmentally friendly tannic acid multilayer coating for reducing corrosion of carbon steel. *Ind. Eng. Chem. Res.* **2021**, 60, 243–250.

(S28) Khosravi H, S.; Veerapandiyan, V. K.; Vallant, R.; Reichmann, K. Effect of processing conditions on the structural properties and corrosion behavior of TiO_2-SiO_2 multilayer coatings derived via the sol-gel method. *Ceram. Int.* **2020**, 46, 17741–17751.

(S29) Dezfuli, S. M.; Sabzi, M. Effect of yttria and benzotriazole doping on wear/corrosion responses of alumina-based nanostructured films. *Ceram. Int.* **2018**, 44, 20245–20258.

(S30) Bernasconi, R.; Panzeri, G.; Firtin, G.; Kahyaoglu, B.; Nobili, L.; Magagnin, L. Electrodeposition of ZnNi alloys from choline chloride/ethylene glycol deep eutectic

solvent and pure ethylene glycol for corrosion protection. *J. Phys. Chem. B*. **2020**, 124, 10739–10751.

(S31) Salazar-Bravo, P.; Del Angel-López, D.; Torres-Huerta, A. M.; Domínguez-Crespo, M. A.; Palma-Ramírez, D.; Brachetti-Sibaja, S. B.; Ferrel-Álvarez, A. C. Investigation of ZnO/waterborne polyurethane hybrid coatings for corrosion protection of AISI 1018 carbon steel substrates. *Metall. Mater. Trans. A*. **2019**, 50, 4798–4813.

(S32) Mahdavi, S.; Asghari-Alamdari, A.; Zolola-Meibodi, M. Effect of alumina particle size on characteristics, corrosion, and tribological behavior of Co/Al_2O_3 composite coatings. *Ceram. Int.* **2020**, 46, 5351–5359.

(S33) Arora, H. S.; Perumal, G.; Rani, M.; Grewal, H. S. Facile and green engineering approach for enhanced corrosion resistance of $Ni–Cr–Al_2O_3$ thermal spray coatings. *ACS Omega* **2020**, 5, 24558–24566.